PAPER

Check for updates

Temperature dependence in fast-atom diffraction at surfaces

Peng Pan, [ID] Maxime Debiossac [ID] and Philippe Roncin [ID]

Grazing incidence fast atom diffraction at crystal surfaces (GIFAD or FAD) has demonstrated coherent diffraction both at effective energies close to one eV ($\lambda_\perp \approx 14$ pm for He) and at elevated surface temperatures offering high topological resolution and real time monitoring of growth processes. This is explained by a favorable Debye–Waller factor specific to the multiple collision regime of grazing incidence. This paper presents the first extensive evaluation of the temperature behavior between 177 and 1017 K on a LiF surface. Similarly to diffraction at thermal energies (TEAS), an exponential attenuation of the elastic intensity is observed but, contrarily to TEAS, the maximum coherence is not directly reduced by the attraction forces that increase the effective impact energy. It is more influenced by the surface stiffness and appears very sensitive to surface defects.

1 Introduction

The characterization of new materials requires a variety of techniques to analyze their physical and chemical properties. These can be real space microscopic techniques such as scanning tunneling microscopy and atomic force microscopy but also reciprocal space techniques using X-rays, neutrons, electrons, or atoms. Since atoms with kinetic energies below a few eV cannot penetrate below the surface, thermal energies atom scattering (TEAS), also known as helium atom scattering (HAS), is a valuable tool to investigate surfaces and 2D materials.[1,2] It is insensitive to the presence of magnetic or electric fields and does not induce any direct damage or charging of the surface. However, its geometry is not compatible with a standard molecular beam epitaxy (MBE) vessel which requires that no instrument prevents the gas from the evaporation cells from reaching the surface. MBE also requires elevated surface temperatures in order to control the mobility of the deposited atom or molecule so that these can reach an optimum location in a reasonable timescale without being trapped too long in undesirable sites.[3] In this context, grazing incidence fast atom diffraction (GIFAD[4] or FAD[5]) which is the high energy, grazing incidence counterpart of TEAS offers decisive advantages; it has been shown to be compatible with a harsh UHV environment and with the MBE geometry. At variance with TEAS, the full diffraction image can be recorded in seconds so that it can be used as a real time diagnostic of the structure of the terminal layer. More unexpected, diffraction can be recorded on a surface at elevated temperatures. This is illustrated in Fig. 1 taken from ref. 6 and recorded inside a MBE vessel with a GaAs surface at around

850 K, whereas TEAS is mainly performed at low temperatures. This interesting aspect of GIFAD to operate at elevated surface temperatures is poorly documented[7–9] and no systematic experimental investigation has been reported.

This paper presents experimental investigations on temperature dependence under a wide variety of experimental conditions of energy, angle of incidence and temperatures for helium atoms impinging on a LiF surface. The paper is organized as follows, the experimental setup is described in Section 2 with the protocol used to transform raw data into transverse and polar scattering profiles from which the coherence ratio is defined. In Section 3, the strategy adopted to performed stable
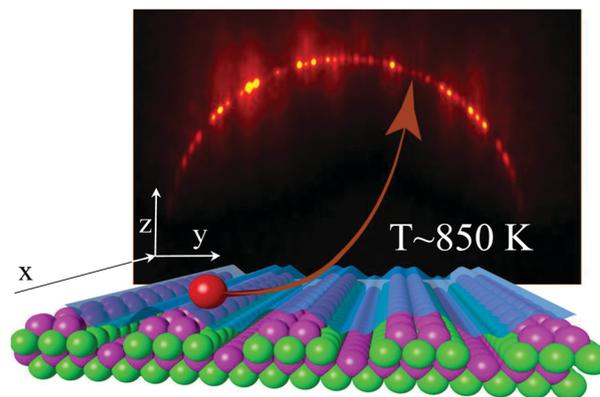
Fig. 1 Schematic view of a GIFAD setup, the well-aligned row of atoms acts as a grating for the projectile atomic wave. A detector located almost a meter downstream records the diffraction image. The one here, taken from ref. 6 was recorded directly in a MBE vessel with 400 eV He at 0.65° on a GaAs(001) surface at ~850 K. The bright spots corresponding to elastic diffraction are located on the Laue circle of energy conservation.

Université Paris-Saclay, CNRS, Institut des Sciences Moléculaires d'Orsay (ISMO), 91405 Orsay, France

temperature variations is presented before an introduction to theoretical aspects of elastic and inelastic diffraction in Section 4. The results are presented and discussed in Section 5.

2 Grazing incidence fast atom diffraction (GIFAD)

The grazing incidence fast atom diffraction at crystal surfaces uses atoms in the keV energy range as probed with incidence angles θ_i around 1 deg. so that the full diffraction pattern can be recorded in one take on a position-sensitive detector[10–13] as sketched in Fig. 1. A commercial ion source delivers ions at the desired energy, they pass inside a charge exchange cell filled with the same gas, where a significant fraction is neutralized by resonant electron capture, see *e.g.* ref. 14. After this cell, the ion fraction is deflected away and the spatial extent and angular divergence of the neutral beam is controlled by two co-linear diaphragms adjustable between 20 and 100 μm, separated by a distance close to half a meter before entering into the UHV chamber with the target. If the projectile encounters a large enough terrace, it undergoes quasi-specular reflection and the projectiles are scattered within a cone with an opening angle of θ_i. Since keV atoms are easily detected and imaged by micro-channel plates, GIFAD was able to record a few images per second[15,16] with an old ion source.

GIFAD offers a high topological resolution of a few *pm* on atomic structure, *e.g.* surface rumpling[17] or charge transfer,[18] simple semi-quantitative interpretation[14] and, when compared with exact quantum scattering code,[4,19–21] a parameter free accuracy.[6,22] The temperature of the surface affects both its nuclear and electronic structures. We use the well-documented system of helium on LiF(001), where the large band-gap prevents electronic contributions,[23,24] at least in the quasi-molecular velocity regime and for normal energy $E_\perp$ below 1 eV. This allows interpretations of inelastic effects only in terms of thermal motion of the surface atoms.

A definition of the (x,y,z) axis is displayed in Fig. 1 together with a typical raw diffraction image on GaAs at elevated temperatures. Another raw diffraction image is plotted in Fig. 2(d) for a LiF crystal and a helium beam oriented along the [110] direction. These images correspond to a direct mapping of the final velocity or wave vector (k_{fy}, k_{fz}) of the scattered projectile perpendicular to the crystal axis. Bright elastic diffraction spots are clearly visible and located on a single circle corresponding to energy conservation of the motion in the (y,z) plane perpendicular to the crystal axis probed: $k_{fy}^2 + k_{fz}^2 = k_\perp^2 = \text{cst.}$ A polar-like transformation[25] brings this Laue circle into a straight line displayed in (Fig. 2(a)). The intensity in this narrow stripe of maximum intensity is reported on Fig. 2(c) and shows well-resolved diffraction peaks equally separated by multiples of the Bragg angle $\theta_B = \arctan(G_y/\hbar k_\parallel)$, where $\hbar k_\parallel = \hbar k \cos\theta_{in}$ is the projectile momentum parallel to the crystal axis. $G_y = 2\pi/a_y$ is the reciprocal lattice vector associated with the distance a_y between atomic rows perpendicular to the probed crystal axis, taken here as the x direction. To derive the structure factor,
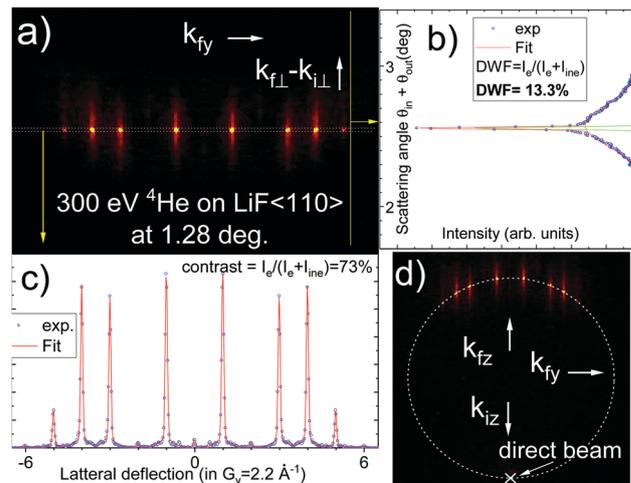

Fig. 2 (a) Quasi polar transform of the raw diffraction image in panel (d). The polar scattering profile (b) corresponds to a full projection of (a) onto the vertical axis. It is fitted by the sum of a narrow Gaussian and a broad log-normal profile used to evaluate the DWF = I_e/I_{tot} with $I_{tot} = I_e + I_{ine}$. Panel (c) corresponds to the intensity in a narrow horizontal band centered at the specular angle. The contrast measured on the Laue circle (c) is 73% much larger than the DWF = 13%.

only the elastic intensities should be considered, however, when elastic intensity is significant, the elastic and inelastic relative intensities on the Laue circle I_m were found identical[26] so that Fig. 2(c) can be directly exploited.

The projection of Fig. 2(a) on the vertical axis produces the polar scattering profile in Fig. 2(b) showing a narrow elastic peak on top of a broader inelastic scattering profile. The relative weight of the elastic peak can be estimated using a simple fit where the elastic component is represented by a narrow Gaussian peak and the inelastic one by a broader, slightly asymmetric log-normal profile $f(\theta) = \dfrac{1}{w\theta\sqrt{2\pi}} \exp\left(-\dfrac{(\ln\theta - \ln\theta_s)^2}{2w^2}\right)$.[27–29] Assuming that the image contains only the gently scattered projectile that did not encounter major surface defects, this ratio DWF = I_e/I_{tot} is believed to be a direct measurement of the Debye-Waller factor. It is slightly different from the standard definition used in TEAS DWF = I_e/I_0 where I_0 would be the intensity scattered from a ideal lattice at rest.[30] The measure of the direct beam intensity[31] could also provide a reference for I_0 to determine absolute diffraction intensities. In GIFAD, the direct beam is always measured, either directly or through a calibrated attenuation grid, because both the exact beam position and line-profile are mandatory for accurate determination of the small angles. It reveals that for the present cleaved LiF sample, the intensity scattered by the surface drops rapidly as the incidence angle is decreased. The reflectivity starts around unity above 2-3 deg and drops down to only a few percent below 0.5 deg. This reduced reflectively is in part due to the overlap with the sample surface but is probably mainly due to the distribution of terrace height resulting from the cleavage.

Fig. 3 shows three diffraction images recorded at temperatures of 177 K, 687 K, and 1017 K measured with a type-N thermocouple mechanically pressed on the backside of the
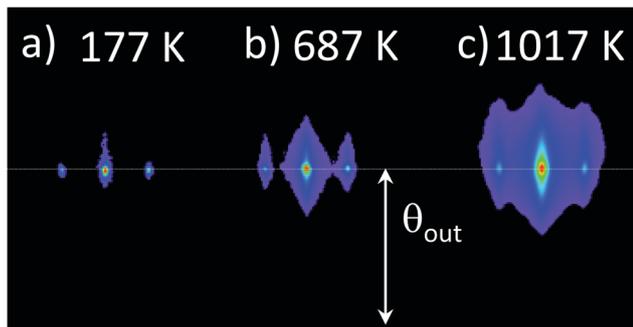
Fig. 3 Three diffraction images recorded with 500 eV helium impinging with θ_{in} = 0.75 deg. on LiF[100] at temperatures of 177 K (a), 687 K (b) and 1017 K (c). The images are normalized to the maximum intensity corresponding here to the elastic specular spot. The rainbow color palettes are identical with a threshold at 3% of the maximum intensity.

sample plate. The transition from a spotty pattern to a much more diffuse one is clearly visible and is discussed in detail along the vertical and horizontal axis corresponding respectively to the polar profile and lateral deflection. On Fig. 4(a) the intensity on the Laue line is displayed in the log scale. Within experimental uncertainty due to slightly different beam conditions, the narrow elastic peaks do not change shape but the inelastic contribution increases both in intensity and in width as outlined by the full lines. More precisely, in this example, both the extrapolated inelastic peak intensity and the exponential decay range increase quasi-linearly with the temperature.

Fig. 4(b) reports the polar scattering profiles of Fig. 3. The broad inelastic profile is also clearly identified with a relative height and a width growing with temperature so that the relative elastic intensity decay rapidly. At this stage, it is useful to compare with the first investigation of the temperature dependence performed when elastic diffraction was not yet demonstrated and where all peak shapes seemed to depend on temperature,[6,18,32] probably because of a limited surface coherence. In this context, the Debye-Waller factor was tentatively attributed to the ratio of the narrow peak relative to the
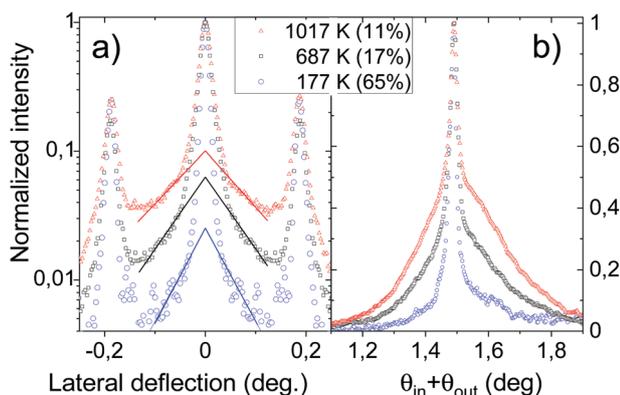
total intensity observed on the Laue circle,[7,33,34] *e.g.* in Fig. 2(b) or Fig. 4(a), rather than from the projected polar profile in Fig. 2(c) or Fig. 4(b). This point of view, obviously underestimates the overall inelastic intensity and strongly depends on the primary beam profile, and is not used anymore. Our ability to isolate the elastic contribution by a fit is limited by experimental aspect such as statistic for the inelastic profile and resolution for the elastic one but also by theoretical limitations that the Log-normal profile is valid only for a single inelastic collision. It seems to remain a good approximation for multiple inelastic collisions, but strictly speaking, the convolution of such profiles is not anymore a log-normal profile.[26,28] In practice we deliberately limit ourselves to elastic contributions above 1% where the elastic peak is still visible.

3 ϕ-scan, θ-scan, E-scan and T-scan

A typical GIFAD experiment begins with the introduction or preparation of a new sample surface and subsequent annealing. The first measurements consist of a rapid azimuthal scan, φ-scan, where the target surface is rotated in-plane (around the z axis in Fig. 1) in order to identify its crystal axis. It does not require that diffraction is observed because a simple analysis of the width of scattered lateral profiles; $\langle k_{fy}^2 \rangle^{1/2}$ in Fig. 2a, c, d and 4a), as a function of the target azimuthal angle φ is enough to identify the principal crystal axis. The procedure called triangulation[14,35,36] is used where the angle of incidence θ ($\equiv k_{iz}$) is kept constant. In practice, measuring the relative width $\langle k_{fy}^2 \rangle^{1/2}/k_{iz}$ compensates for a minor tilt between the surface normal and the rotation axis.[36,37] After proper alignment on the desired axis, the surface is prepared by various methods until a good diffraction pattern is observed. Here, we used LiF single crystal previously irradiated by γ-rays[38] giving a pronounced yellow to orange color, and cleaved in the air just before introduction into the vacuum. Subsequent heating at 400 °C during a few hours is usually enough to recombine the color centers and to record clean diffraction images with well-resolved elastic spots. The size of the diffraction spots provides indications of the surface coherence length. The lateral angular resolution corresponding to 1/10 of the Bragg angle indicating a transverse coherence length $\delta_y = (k\delta\theta)^{-1} \sim 10a$ with a the lattice unit. The equivalent vertical width suggests a longitudinal coherence length δ_z/θ_{in} almost hundred times larger for θ = 0.57 deg so that $1/\theta$ = 100 (for circular diaphragms $\delta k_z = \delta k_y$ so that $\delta_z = \delta_y$). Thus coherent specular reflection requires a crystal without defect on a surface δ_S given by $10^4 a^2$ equivalent to a tiny square hundred by hundred lattice units or 10^5 Å^2.

In principle, a T-scan would consist of a simple variation of the target temperature leaving all other parameters unchanged. Unfortunately, this is not compatible with the extreme sensitivity of grazing incidence. In GIFAD, the target surface is easily positioned within 10 to 20 m from the beam: when it is not inserted enough, the primary beam is still present on the image, whereas when it is inserted too much, the direct beam impacts the edge of the $\approx$1 mm thick crystal and even the scattered beam disappears from the detector. However, thermal

Fig. 4 For the three images in Fig. 3, panel (a): lateral profiles on the Laue circle, the lines are here to outline the exponential decay of the peak tail. Panel (b): Polar scattering profiles. The measured values of the DWF are reported in parenthesis and also plotted in Fig. 8(a).

This journal is © the Owner Societies 2022

Phys. Chem. Chem. Phys., 2022, **24**, 12319–12328 | **12321**

expansion of the target crystal and of the manipulator induce much larger displacements as well as minor angular tilts producing major effects in GIFAD (see *e.g.* the θ^3 dependence in Fig. 7). For this reason, we were not able to record the three images displayed in Fig. 3 one after the other. Instead, we had to wait for a stable temperature before realigning the target and restoring a comparable incidence angle. In the following, we rationalize this approach by performing several θ-scan or *E*-scan at different temperatures. From these variations, we interpolate between measured angular values, for instance with a B-spline, to restore a temperature variation. It should be noted that at elevated temperatures, typically above 800 K, particles emitted from the heating filament produce an additional noise on our detector that may ruin a temperature variation whereas, taking time to find a stable detector bias and data-acquisition-mode can reduce the noise level allowing a more stable θ-scan or *E*-scan.

4 Elastic and inelastic diffraction

For ideal crystalline surfaces with atoms at the equilibrium position, it has been shown that the rapid movement parallel to the crystal axis (x) is decoupled from the slow one in the (y,z) perpendicular plane.[20,21,39–42] Therefore, elastic diffraction of fast atoms along a crystal axis is equivalent to that of a much slower particle with an energy $E_\perp = E\sin^2\theta$ evolving in the averaged potential $V_{2D}(y,z) = \int_x V_{3D}(x,y,z)$. Experimentally, this axial channeling approximation (ASCA) results in diffraction taking place only in the (y,z) perpendicular plane[14,40,43] (see also[32,39] for the cases where the ASCA breaks down.). From a spatial point of view, the elastic diffraction can be seen as the coherent part of the scattered waves and this later can only build up at a location corresponding to the equilibrium position, the one of the center of the vibrational wavefunction. In contrast, inelastic diffraction corresponds to a situation where momentum and/or energy has been exchanged with the surface *i.e.* with the vibration of the surface atoms or phonons, breaking the exact translation symmetry of the ideal surface and requiring *a priori* to abandon the ASCA for a full 3D representation.[8,9]

In TEAS, X-ray or neutron diffraction, this situation is described by the Debye-Waller factor $DWF = I_e/I_0 = e^{-\sigma_\varphi^2}$ where σ_φ^2 is the variance of the phase distribution induced the thermal displacement σ_z of surface atoms. In a Debye model of solids, each atom is described by a local harmonic oscillator with frequency ω_D and the thermal amplitude is Gaussian $\sigma_z(T)$ resulting in a phase coherence $e^{-\sigma_\varphi^2} = e^{-q^2\sigma_z^2}$ where q is the projectile momentum. It describes how the elastic diffraction intensity progressively vanishes when the amplitude σ_z of the thermal disorder becomes comparable to the projectile wavelength $\lambda = h/q$. From a momentum point of view, the DWF can be written as $e^{-E_r/\hbar\omega}$ where $E_r = q^2/2m$ is the binary recoil energy, which can be interpreted as the Lamb-Dicke probability of recoil-less emission that the harmonic oscillator exchanges the momentum $2q$ without changing its energy level. This DWF

does not apply directly to GIFAD, even when considering $\lambda_p = \lambda/\sin\theta_{in} \gg \lambda$, because the momentum exchange of $2k\sin\theta_{in}$ needed for specular reflection of the primary beam is acquired *via* several successive fast gentle collisions with surface atoms. With a rigid lattice model and an exponential repulsive mean planar potential of stiffness Γ, $V(z) = V_0 e^{-\Gamma z}$, the trajectory is analytic and the binary momentum exchanges can be calculated to obtain the classical energy loss ΔE_{Cl} in eqn (1) with m_p the projectile mass and a the lattice unit.[26,28] The effective number $N = \dfrac{6}{\Gamma a\theta}$ of binary collision is defined such that N times the individual deflection $d\theta$ is the specular deflection $2\theta_{in}$ and that N times the individual binary recoil energy E_r matches the analytic total energy loss $\Delta E_{Cl} = NE_r$. The DWF for GIFAD writes:

$$DWF = \exp\left(-\frac{3\Delta E_{Cl}}{\hbar\omega_D}\coth\frac{T_D}{2T}\right), \ \Delta E_{Cl} = \frac{2m_p}{3m}E\Gamma a\theta_i^3 \equiv NE_r \tag{1}$$

For the He-LiF system, the product Γa is close to $14^{22,29}$ so that $N \approx 2/\theta$ can be large explaining why elastic diffraction could be observed with $E_\perp$ close to one eV[14,43] whereas TEAS is usually limited below 100 meV. Alternately, with this reduced decoherence, GIFAD can explore the higher temperatures that are needed for MBE.

This naive, purely repulsive description was improved by taking into account an attractive part of the potential, for instance, van der Waals contributions,[44–47] responsible for the physisorption well of depth D. In elastic diffraction, the effect of such attraction is the presence of bound-state resonances[48,49] and the increase of the rainbow angle at low energy.[22] These are naturally accounted for using a quantum approach[22,49] or modeled in semi-classical[50] or optical method such as the hard corrugated wall by the Beeby correction indicating that the effective impact energy $E_\perp$ increases to $E_\perp + D^{44,51,52}$ or considering a modified angle of incidence $\theta_{eff} = \sqrt{\theta_{in}^2 + D/E}$. The Beeby correction also decreases significantly the DWF in TEAS.[53] In GIFAD, we also found that the mere presence of a tiny well significantly modifies the stiffness of the potential by bringing the turning point much closer to the surface plane.[29] This can be expressed quantitatively using a Morse potential $V_M(z) = D(e^{-\Gamma(z-z_0)} - 2e^{-\Gamma/2(z-z_0)})$ and looking for the turning point z_t where $V_M(z_t) = E_\perp$ the effective stiffness is:

$$\Gamma_{eff}(E_\perp) = \Gamma\left[1 + \left(1 + \frac{E_\perp}{D}\right)^{-1/2}\right] \tag{2}$$

This increased stiffness was already identified in TEAS[54] but it has much less consequence since at normal incidence the projectile hits a single surface atom, only the time scale $\tau \approx \Gamma/v_{//}$ depends on Γ not the magnitude of the exchanged momentum $2q$ and therefore not the coherence ratio. It is the reverse in grazing scattering, for identical values of $E_\perp$ the time scale for bouncing from the surface are identical in TEAS or GIFAD, but the time needed for a single quasi binary collision is now independent on Γ_{eff}, while its magnitude $\approx 2q/N$ depends directly on the effective stiffness Γ_{eff}. In summary, for GIFAD,

12322 | *Phys. Chem. Chem. Phys.*, 2022, **24**, 12319–12328

This journal is © the Owner Societies 2022

the stiffness Γ_{eff} governs the momentum transferred in each collision, a stiffer interaction potential needs fewer collisions for specular reflection and each of them becomes more violent leading to an overall reduction of the DWF.

At the atomic level, the temperature is modeled by the spatial extend of a surface atom of mass m, which, in a Debye harmonic model is Gaussian profile with $\sigma_z^2(T) = \dfrac{3\hbar}{2m\omega}$ $\coth\dfrac{T_D}{2T} \sim \dfrac{3\hbar}{2m\omega}\dfrac{2T}{T_D}$, where T_D is the Debye temperature such that $\hbar\omega = k_B T_D$ with k_B the Boltzmann constant.

5 Results

5.1 Orientation of the surface

When investigating the polar scattering profile,[29] it was shown that the shape of the polar scattering profile does not depend significantly on the orientation of the surface. This is illustrated in Fig. 5 and we have checked that this similarity remains valid at different temperatures. Since both the data acquisition and the data analysis are simpler for random orientation of the surface where only one specular order ($m = 0$) is present, most of the temperature variations presented here correspond to this crystal orientation. The other data were recorded along the [100] direction where the corrugation amplitude is reduced generating fewer diffraction orders as visible when comparing Fig. 5a with Fig. 5b.

5.2 Bragg angle and form factor

The main focus of this paper is the temperature dependence of the elastic ratio which is presumed to depend mainly on the thermal movement of the surface atoms. When analyzing the intensity on the Laue circle as displayed in Fig. 2c), we can extract the value of the Bragg angle as well as the relative intensities I_m associated with each diffraction order m. Both
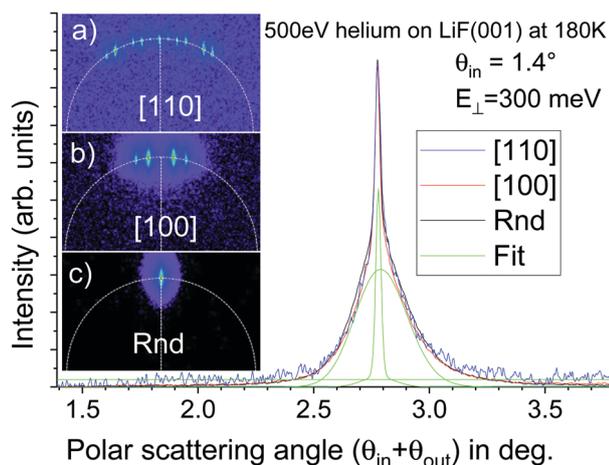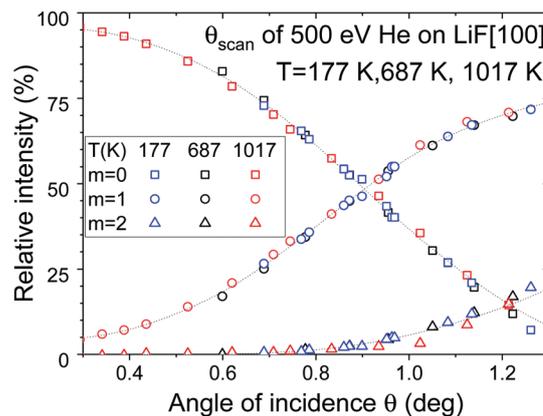

Fig. 6 The relative intensities I_m of (black) $m = 0$, (black) $m = \pm 1$ and (Δ)$m = \pm 2$ extracted from the elastic intensities recorded in three θ-scan performed at temperatures of ○ 177 K, ○ 687 K, ○ 1017 K, fall on top of each other.

could change with the temperature due to thermal expansion and possible reconstruction of the surface. This could be investigated in detail but we have only checked that the surface equilibrium positions and GIFAD form factor do not change significantly. The evolution of the Bragg angle is compatible with the thermal expansion coefficient measured by TEAS[55] and the Fig. 6 shows that in spite of important variation of the scattering profiles visible in Fig. 3 and 4, the relative intensities I_m measured along the [100] direction do not change significantly with temperature. This aspect is not discussed further because, in practice, it is by-passed when analyzing the random direction where the reciprocal lattice vector is absent.

5.3 Sample quality

All our samples have been prepared by cleaving at air LiF crystals previously irradiated by γ rays,[38] however, the Debye-Waller factor varies from sample to sample and also depend on the actual part of the surface illuminated by the atomic beam. As a worst case, we experienced a variation up to almost a factor two, after changing the target orientation and position when switching from Random to [100] direction. Exploring a few target positions is usually enough to optimize the DWF. We also observed a slow degradation of the diffraction images with time even at a few 10^{-10} mb pressure. When taking a sample that was left in a vacuum for a few weeks, the measured DWF is systematically lower, even after a short thermal treatment. This is illustrated in Fig. 7 where three sets of data recorded on different samples are reported. In spite of a scattering of data points in each set, the data follow different curves and therefore different DWF, but the trends are similar. In the final analysis, we have kept only two samples with large enough temperature variations and we provide the results as separate sets.

5.4 Energy and angular variations

As detailed in Section 4, the effective DWF adapted to GIFAD is expected to scale with $\exp(-E\theta_{in}^3)$ where E is the primary beam

Fig. 5 (a–c) are raw diffraction images of 500 eV helium incident at 1.4° on LiF at 180 K oriented along the [110], [100], and random direction, respectively (in part, taken from[29]). The resulting polar scattering profiles are almost identical, with a narrow elastic peak at $\theta_{out} = \theta_{in}$ on top of a broader peak fitted by a log-normal profile[27] (green curves).
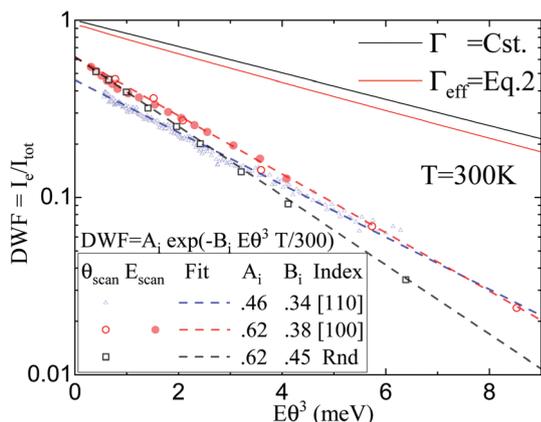
Fig. 7 The DWF = DWF = $\frac{I_e}{I_i}$ from 3 LiF samples are reported as a function of $E\theta^3$. The dotted lines are fits to the data while the solid lines are numerical prediction of eqn (1) with (red A = 0.94, B = 0.19) and without corrections (black A = 1, B = 0.17) due to the attraction towards the surface.

energy and θ_{in} the angle of incidence. This was suggested from the spatial approach[7] considering that the scattering by a row of N atoms should have a mean thermal amplitude $\langle\sigma_z^2\rangle = \sigma_z^2/N$ or from momentum transfer along the trajectory[26,28] because the classical recoil energy loss is also expected to scale with $E\theta_{in}^3$. This dependence was first observed at room temperature by reporting DWF measured on a large set of energy and

incidence angles.[29] The Fig. 8(a and c) display similar dependence's recorded during E-scan and θ-scan at different temperatures. All curves indicate a pronounced exponential decay illustrated by the straight lines resulting from independent fits DWF = $A_i\exp\left(-B_iE\theta^3T/300\right)$ where both A_i and B_i were left free and without any weighting of the data.

5.5 Temperature dependence

According to the announced strategy, we do not use the fits of Fig. 8(a) to evaluate the temperature dependence but we use the B-spline interpolation of the data, plotted as dotted lines Fig. 8(a) to produce the temperature dependence displayed in Fig. 8(b) at fixed values of $E\theta^3$ between 0.5 meV and 6 meV. Here again, the exponential character is readily visible. In contrast with Fig. 8(a), we now try to apply a unique formula to describe all the data. The adjustment was performed by changing step-wise the parameters A and B until a decent visual impression is obtained. In practice, we could have used the data from the fits through the $E\theta^3$ variation Fig. 8(a and c) but this would induce a possible bias forcing the final dependence.

In TEAS, the Beeby correction to the DWF alone is significant and limits the maximum coherence, it is often used to estimate the D value (see $e.g.$[2,44,56]). This is not the case in GIFAD, a numerical evaluation, reported as full lines in Fig. 7 indicates that these corrections have a weak influence both on the magnitude and the exponential range.
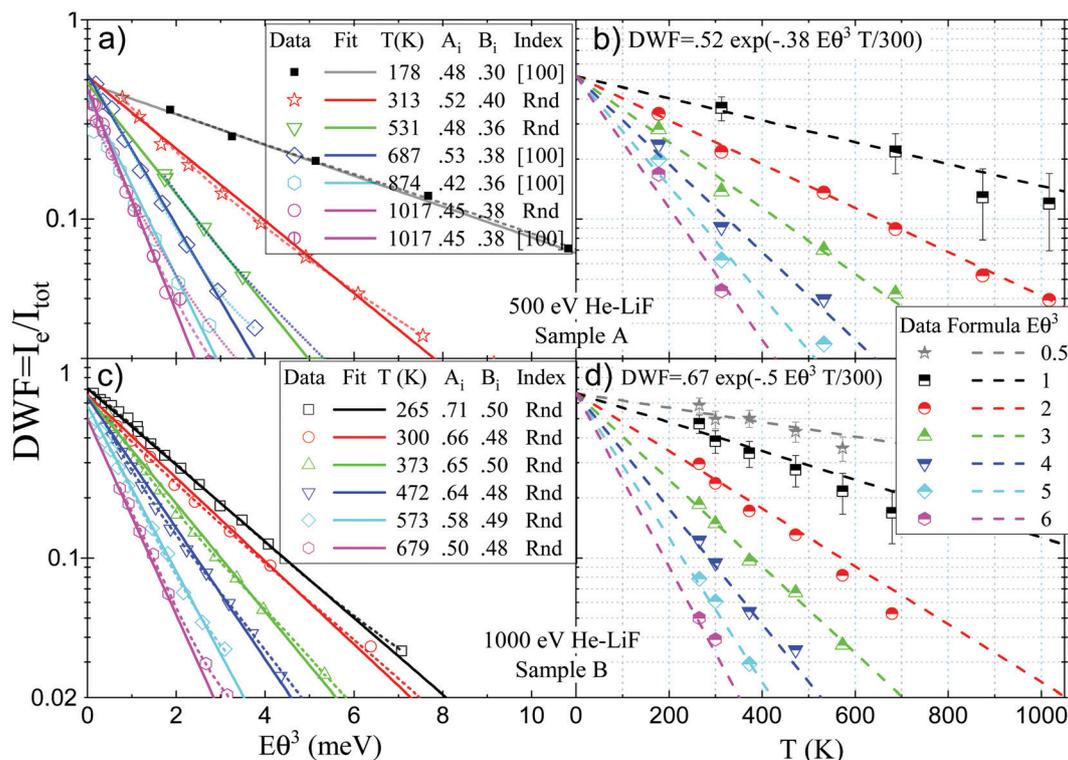

Fig. 8 Panels (a and c), report the DWF as a function of the reduced parameter $E\theta^3$ for two different LiF samples. The dotted lines are B-spline interpolation used to derive the temperature dependence at fixed values of $E\theta^3$ in (b and d) and reproduced by a global formula. At very low angles of incidence, corresponding to $E\theta^3 \leq 1$ meV, where a diffuse scattering background is present an error bar estimated to 5% is plotted.

12324 | *Phys. Chem. Chem. Phys.*, 2022, **24**, 12319–12328

This journal is © the Owner Societies 2022

5.6 The inelastic scattering width

The polar inelastic scattering profile is fitted log-normal form[27] and the relative width w are reported in Fig. 9(a and b) as a function of the perpendicular energy $E_\perp$, a quantity that governs the distance of closest approach to the surface. The fact that this width was found[29] to depend mainly on $E_\perp = E\theta^2$ indicates that it is sensitive to the magnitude of the most violent inelastic collisions along the trajectory rather than to the integral effect of such collision which would be closer to $E\theta^3$. Assuming that the inelastic collision is well-modeled by classical mechanics, the thermal motion $\sigma_z(T)$ of the surface atom induces, for each collision a log-normal scattering profile having a width $dw = \Gamma\sigma_z$[26,28] or, equivalently a contribution to the angular straggling $d\sigma_\theta = \Gamma\sigma_z d\theta$ where $d\theta$ is the elastic deflection angle in this collision already estimated as $d\theta = (\theta_{in} + \theta_{out})/N$. Adding the N individual variances $d\sigma_\theta^2$ or using the mean log-normal width $w = dw/\sqrt{N}$ the classical scattering width is predicted:

$$w_{Cl} = \Gamma\sigma_z/\sqrt{N}, \text{ with } N = 6/\Gamma a\theta_{in} \qquad (3)$$

The comparison with experiment is tricky, the eqn (3) reproduced the evolution during an E-scan but not during a θ-scan while the experiment gives similar results during E-scan and θ-scan.[29] In this respect, the following discussion is only qualitative. More precisely, during an E-scan where θ_i is fixed N would stay constant so that, neglecting here the Beeby correction, $w_{Cl} \propto \Gamma\sigma_z$ would remain constant. However, as already observed at room temperature[29] and in Fig. 9(a and b) a sharp increase of w is observed at low $E_\perp$. The agreement was established by taking into account the attractive forces *i.e.* by replacing Γ by Γ_{eff} from eqn (2). The increase at low energy could be then be attributed to the enhanced stiffness at low energy.[29] The full, dashed and dotted lines indicate how the absolute values of w_{Cl} depend on the angle of incidence of the hypothetical equivalent E-scan. The 5.5c) reports the value of w measured at $E_\perp = 500$ meV where is becomes stable. The lines using the same eqn (3) now indicate that the evolution of the

plateau values in Fig. 9(a and b) is compatible with the expected variation of σ_z even if the low-temperature zero point motion (green curve) is not visible. The physical parameter $D = 8.5$ meV[48] and $T_D = 550$ K[17] correspond to well-accepted values in the literature and $\Gamma = 3.5$ Å^{-1} was derived in a quantum calculation.[49] It is close to the asymptotic value $\Gamma = 2\sqrt{2W} = 3.55 \pm 0.15$ Å^{-1} where $W = 12.2 \pm 0.5$ eV is the work-function of LiF. Once again, the semi-quantitative agreement should be balanced by the fact that the model does not predict the observed similar behavior of $w(E_\perp)$ during an E-scan and a θ-scan.

6 Discussion

With the LiF samples used here, the Fig. 8(b and d) indicate that GIFAD is not able to provide an internal value of the temperature with an accuracy better than 20–50 °C. Combining consistently the width w and the DWF could improve the accuracy but the sensitivity to sample quality appears as a severe limitation. In contrast, if the main focus is to optimize the growth parameters to improve the surface quality in terms of coherence length, *i.e.* mean distance L_C between defects, GIFAD offers a unique handle with a very broad range of operation. First, a simple φ-scan[36] can identify crystallographic axis even without diffraction offering a first estimate of L_C *via* the peak to background ratio of the φ-scan.[14] When diffraction becomes visible, the presence of elastic diffraction, and its associated elastic peak width, readily gives insights on L_C. Then, optimizing the DWF could give real time access to very large defect-free surfaces with the advantage that the diagnostic is performed simultaneously on an illuminated surface $S \approx \varnothing^2/\theta$ on the order of 1 mm^2 for a diaphragm size of $\varnothing = 100$ μm. This diagnostic is complementary to the elastic diffracted intensity which indicates in real time the detailed topology of the terminal layer. We have shown here that the width w of the scattering profile can be understood qualitatively in terms of a classical model using an effective stiffness $\Gamma_{eff}(E_\perp)$ and a thermal amplitude $\sigma_z(T)$. This suggests that classical scattering simulation in
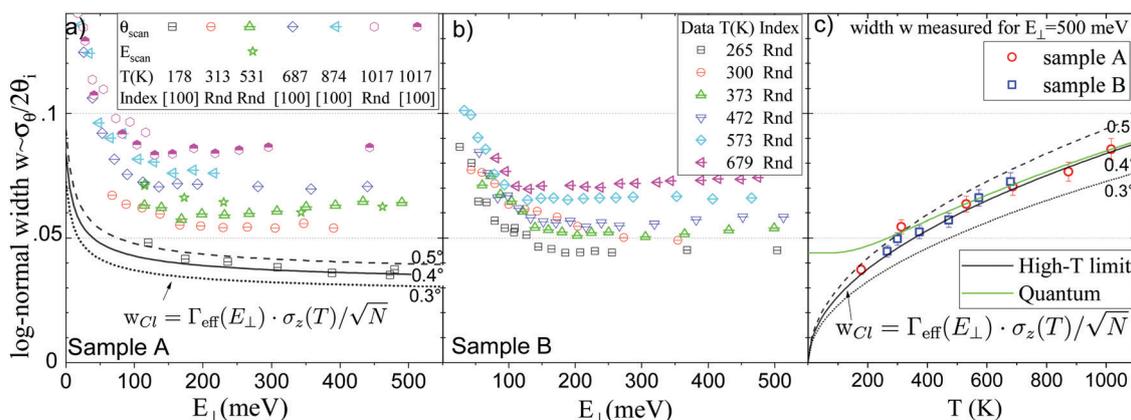

Fig. 9 (a and b) inelastic scattering width w as a function of $E_\perp = E\theta^2$. The increase at low $E_\perp$ is mainly due to $\Gamma_{eff}(E_\perp)$. The w measured at the asymptotic value $E_\perp = 500$ meV are reported in panel (c) with the mean thermal amplitude $\sigma_z^2(T)$. The lines in (a and c) correspond to eqn (3) with different angles in the evaluation of N. (see text) The green curve marked as Quantum takes the zero point energy into account.

This journal is © the Owner Societies 2022

Phys. Chem. Chem. Phys., 2022, **24**, 12319–12328 | **12325**

grazing incidence, in general[57] and in the context of GIFAD[8,9] should produce a fair estimate of the inelastic profile. However, *In fine*, a quantum inelastic treatment as developed in TEAS[58] and recent attempts to encompass both elastic and inelastic aspects under grazing incidence[59] should help connecting to the real world of surface phonons and their possible specific coupling to the multiple collision regime.

7 Conclusions

Using a definition based on the analysis of the polar scattering profile to isolate the elastic and inelastic components, the DWF can be evaluated for each diffraction image. At comparable energy and incidence angle, the DWF is found to be independent of the crystal axis probed. Due to the extreme sensitivity to mechanical deformations associated with temperature variations, the T-scans were performed indirectly *via* interpolation of θ-scan and E-scan at different temperatures. At each temperature, the DWF specific to the multiple collision regime of GIFAD is shown to depend primarily on $E\theta^3$, differing from $E\theta^2$ in TEAS where a single collision regime prevails. Within the present accuracy, a simple exponential decay with temperature is observed but, different LiF samples produce slightly different decay parameters and maximum coherence suggesting an important contribution of the defect density and terrace size distribution. The effect of the attractive forces towards the surface have been investigated in TEAS. It produces an increased impact energy, known as the Beeby correction, and an increased stiffness of the surface mean-planar potential-energy-surface due to a closer distance of approach towards the surface.[54] They also have the same consequences regarding the elastic diffracted intensities in GIFAD or TEAS but very different consequences in the inelastic behavior of GIFAD and TEAS. In TEAS, the Beeby correction is known to limit the maximum possible DWF[44] while in GIFAD, the eqn (1) and Fig. 7c) indicate only a weak influence on the maximum DWF. As to the effective stiffness Γ_{eff},[54] it does not directly affect the DWF in TEAS, whereas, it enters the DWF factor in GIFAD because each binary collision becomes more violent as evidenced by the sharp increase of the inelastic scattering width w at low values of $E\theta^2$ in Fig. 9(a and b). The effect of Γ_{eff} on the DWF, though larger than the Beeby correction is also limited because it is, in part, balanced by the reduced number of collisions needed for specular reflection. Our results also suggest an important contribution of surface defect to decoherence in grazing conditions but this aspect is yet unexplored.

Conflicts of interest

There are no conflicts to declare.

Acknowledgements

References

1 G. Anemone, A. Al Taleb, G. Benedek, A. Castellanos-Gomez and D. Farías, Electron-phonon coupling constant of 2H-MoS$_2$ (0001) from helium-atom scattering, *J. Phys. Chem. C*, 2019, **123**(6), 3682–3686.

2 A. Tamtögl, A. Ruckhofer, D. Campi, W. Allison and W. E. Ernst, Atom-surface van der Waals potentials of topological insulators and semimetals from scattering measurements, *Phys. Chem. Chem. Phys.*, 2021, **23**, 7637–7652.

3 V. Romankov and J. Dreiser, Morphology of ultrathin lithium fluoride deposited on ag(100): Dendrites versus islands, *Phys. Rev. B*, 2021, **104**, 195401.

4 P. Rousseau, H. Khemliche, A. G. Borisov and P. Roncin, Quantum scattering of fast atoms and molecules on surfaces, *Phys. Rev. Lett.*, 2007, **98**, 016104.

5 A. Schüller, S. Wethekam and H. Winter, Diffraction of fast atomic projectiles during grazing scattering from a LiF(001) surface, *Phys. Rev. Lett.*, 2007, **98**, 016103.

6 M. Debiossac, A. Zugarramurdi, H. Khemliche, P. Roncin, A. G. Borisov, A. Momeni, P. Atkinson, M. Eddrief, F. Finocchi and V. H. Etgens, Combined experimental and theoretical study of fast atom diffraction on the $_2$(2 × 4) reconstructed GaAs(001) surface, *Phys. Rev. B: Condens. Matter Mater. Phys.*, 2014, **90**, 155308.

7 P. Rousseau, H. Khemliche, N. Bundaleski, P. Soulisse, A. Momeni and P. Roncin, Surface analysis with grazing incidence fast atom diffraction (GIFAD), *J. Phys.: Conf. Ser.*, 2008, **133**, 012013.

8 L. Frisco and M. S. Gravielle, Phonon contribution in grazing-incidence fast atom diffraction from insulator surfaces, *Phys. Rev. A*, 2019, **100**, 062703.

9 L. Frisco and M. S. Gravielle, Thermal effects on helium scattering from LiF(001) at grazing incidence, *Phys. Rev. A*, 2020, **102**, 062821.

10 V. A. Morosov, A. Kalinin, Z. Szilagyi, M. Barat and P. Roncin, 2π spectrometer: A new apparatus for the investigation of ion surface interaction, *Rev. Sci. Instrum.*, 1996, **67**(6), 2163.

11 J. S. Lapington, A comparison of readout techniques for high-resolution imaging with microchannel plate detectors, *Nucl. Instrum. Methods Phys. Res., Sect. A*, 2004, **525**(1), 361–365.

12 S. Lupone, S. Damoy, A. Husseen, N. Briand, M. Debiossac, S. Tall and P. Roncin, Note: A large open ratio, time, and position sensitive detector for time of flight measurements, *Rev. Sci. Instrum.*, 2015, **86**(12), 126115.

13 S. Lupone, P. Soulisse and P. Roncin, A large area high resolution imaging detector for fast atom diffraction, *Nucl. Instrum. Methods Phys. Res., Sect. B*, 2018, **427**, 95–99.

12326 | *Phys. Chem. Chem. Phys.*, 2022, **24**, 12319–12328

This journal is © the Owner Societies 2022

14 M. Debiossac, P. Pan and P. Roncin, Grazing incidence fast atom diffraction, similarities and differences with thermal energy atom scattering (TEAS), *Phys. Chem. Chem. Phys.*, 2021, **11**(12), 4564–4569.

15 P. Atkinson, M. Eddrief, V. H. Etgens, H. Khemliche, M. Debiossac, A. Momeni, M. Mulier, B. Lalmi and P. Roncin, Dynamic grazing incidence fast atom diffraction during molecular beam epitaxial growth of GaAs, *Appl. Phys. Lett.*, 2014, **105**(2), 021602.

16 M. Debiossac, P. Atkinson, A. Zugarramurdi, M. Eddrief, F. Finocchi, V. H. Etgens, A. Momeni, H. Khemliche, A. G. Borisov and P. Roncin, Fast atom diffraction inside a molecular beam epitaxy chamber, a rich combination, *Appl. Surf. Sci.*, 2017, **391**, 53–58.

17 A. Schüller, S. Wethekam, D. Blauth, H. Winter, F. Aigner, N. Simonović, B. Solleder, J. Burgdörfer and L. Wirtz, Rumpling of LiF(001) surface from fast atom diffraction, *Phys. Rev. A: At., Mol., Opt. Phys.*, 2010, **82**, 062902.

18 H. Khemliche, P. Rousseau, P. Roncin, V. H. Etgens and F. Finocchi, Grazing incidence fast atom diffraction: An innovative approach to surface structure analysis, *Appl. Phys. Lett.*, 2009, **95**(15), 151901.

19 F. Aigner, N. Simonović, B. Solleder, L. Wirtz and J. Burgdörfer, Suppression of decoherence in fast-atom diffraction at surfaces, *Phys. Rev. Lett.*, 2008, **101**, 253201.

20 A. Zugarramurdi and A. G. Borisov, Transition from fast to slow atom diffraction, *Phys. Rev. A: At., Mol., Opt. Phys.*, 2012, **86**, 062903.

21 A. S. Muzas, F. Gatti, F. Martín and C. Díaz, Diffraction of H from LiF(001): From slow normal incidence to fast grazing incidence, *Nucl. Instrum. Methods Phys. Res., Sect. B*, 2016, **382**, 49–53.

22 M. Debiossac, P. Roncin and A. G. Borisov, Refraction of fast Ne atoms in the attractive well of a LiF surface, *J. Phys. Chem. Lett.*, 2020, **11**(12), 4564–4569.

23 H. Winter, Collisions of atoms and ions with surfaces under grazing incidence, *Phys. Rep.*, 2002, **367**(5), 387–582.

24 P. Roncin, J. Villette, J. P. Atanas and H. Khemliche, Energy loss of low energy protons on LiF(100): Surface excitation and *H*-mediated electron emission, *Phys. Rev. Lett.*, 1999, **83**, 864–867.

25 M. Debiossac and P. Roncin, Image processing for grazing incidence fast atom diffraction, *Nucl. Instrum. Methods Phys. Res., Sect. B*, 2016, **382**, 36–41.

26 P. Roncin and M. Debiossac, Elastic and inelastic diffraction of fast atoms, Debye-Waller factor, and Mössbauer-Lamb-Dicke regime, *Phys. Rev. B*, 2017, **96**, 035415.

27 *log-normal distribution.* $f(x) = \frac{1}{xw\sqrt{2\pi}} \exp\left(\frac{(\ln x - \mu)^2}{2W^2}\right)$.

28 J. R. Manson, H. Khemliche and P. Roncin, Theory of grazing incidence diffraction of fast atoms and molecules from surfaces, *Phys. Rev. B: Condens. Matter Mater. Phys.*, 2008, **78**, 155408.

29 P. Pan, M. Debiossac and P. Roncin, Polar inelastic profiles in fast-atom diffraction at surfaces, *Phys. Rev. B*, 2021, **104**, 165415.

30 D. Farias and K.-H. Rieder, Atomic beam diffraction from solid surfaces, *Rep. Prog. Phys.*, 1998, **61**(12), 1575–1664.

31 P. Sutter, M. Minniti, P. Albrecht, D. Farías, R. Miranda and E. Sutter, A high-reflectivity, ambient-stable graphene mirror for neutral atomic and molecular beams, *Appl. Phys. Lett.*, 2011, **99**(21), 211907.

32 M. Busch, J. Seifert, E. Meyer and H. Winter, Evidence for longitudinal coherence in fast atom diffraction, *Phys. Rev. B: Condens. Matter Mater. Phys.*, 2012, **86**, 241402.

33 N. Bundaleski, P. Soulisse, A. Momeni, H. Khemliche and P. Roncin, Decoherence in fast atom diffraction from surfaces, *Nucl. Instrum. Methods Phys. Res., Sect. B*, 2011, **269**(11), 1216–1220.

34 Please note that, when reproducing the Fig. 7 of ref. 7 in ref. 33 the data column was mistakenly replaced by the line to guide the eyes giving an impression of being perfectly aligned, the error was reproduced in ref. 43.

35 F. E. Feiten, J. Seifert, J. Paier, H. Kuhlenbeck, H. Winter, J. Sauer and H.-J. Freund, Surface structure of V_2O_3 revisited, *Phys. Rev. Lett.*, 2015, **114**, 216101.

36 N. Kalashnyk, H. Khemliche and P. Roncin, Atom beam triangulation of organic layers at 100 mev normal energy: self-assembled perylene on Ag(110) at room temperature, *Appl. Surf. Sci.*, 2016, **364**, 235–240.

37 M. Sereno, S. Lupone, M. Debiossac, N. Kalashnyk and P. Roncin, Active correction of the tilt angle of the surface plane with respect to the rotation axis during azimuthal scan, *Nucl. Instrum. Methods Phys. Res., Sect. B*, 2016, **382**, 123–126.

38 J. J. Gilman, C. Knudsen and W. P. Walsh, Cleavage cracks and dislocations in LiF crystals, *J. Appl. Phys.*, 1958, **29**(4), 601–607.

39 A. Zugarramurdi and A. G. Borisov, When fast atom diffraction turns 3D, *Nucl. Instrum. Methods Phys. Res., Sect. B*, 2013, **317**, 83–89.

40 D. Farías, C. Díaz, P. Nieto, A. Salin and F. Martín, Pronounced out-of-plane diffraction of H_2 molecules from a Pd(111) surface, *Chem. Phys. Lett.*, 2004, **390**(1), 250.

41 M. Debiossac and P. Roncin, Atomic diffraction under oblique incidence: An analytical expression, *Phys. Rev. A: At., Mol., Opt. Phys.*, 2014, **90**, 054701.

42 D. M. Danailov and D. S. Karpuzov, Total reflection of energetic ions from crystal surfaces at glancing incidence, *Can. J. Phys.*, 1997, **75**(4), 197–209.

43 H. Winter and A. Schüller, Fast atom diffraction during grazing scattering from surfaces, *Prog. Surf. Sci.*, 2011, **86**(9), 169–221.

44 J. L. Beeby and L. Dobrzynski, The scattering of atoms from surfaces: a model, *J. Phys. C-Solid State Phys.*, 1971, **4**(11), 1269–1278.

45 G. A. Bocan, J. D. Fuhr and M. S. Gravielle, van der Waals effects on grazing-incidence fast-atom diffraction for H on LiF(001), *Phys. Rev. A*, 2016, **94**, 022711.

46 M. del Cueto, A. S. Muzas, G. Füchsel, F. Gatti, F. Martín and C. Díaz, Role of van der Waals forces in the diffraction of noble gases from metal surfaces, *Phys. Rev. B*, 2016, **93**, 060301.

This journal is © the Owner Societies 2022

Phys. Chem. Chem. Phys., 2022, **24**, 12319–12328 | 12327

47 M. S. Gravielle, J. E. Miraglia and G. A. Bocan, *Interaction potentials for atoms in front of a LiF(001) surface*, 2019, ch. 7, pp. 177–203.

48 A. P. Jardine, S. Dworski, P. Fouquet, G. Alexandrowicz, D. J. Riley, G. Y. H. Lee, J. Ellis and W. Allison, Ultrahigh-resolution spin-echo measurement of surface potential energy landscapes, *Science*, 2004, **304**(5678), 1790.

49 M. Debiossac, A. Zugarramurdi, P. Lunca-Popa, A. Momeni, H. Khemliche, A. G. Borisov and P. Roncin, Transient quantum trapping of fast atoms at surfaces, *Phys. Rev. Lett.*, 2014, **112**, 023203.

50 G. A. Bocan, H. Breiss, A. Szilasi, S. Momeni, E. M. Staicu-Casagrande, E. A. Sánchez, M. S. Gravielle and H. Khemliche, Dynamical effects as a window into van der Waals interactions in grazing-incidence fast He-atom diffraction from KCl, *Phys. Rev. B*, 2021, **104**, 235401.

51 A. Al Taleb, G. Anemone, L. Zhou, H. Guo and D. Farías, Diffraction of CH_4 from a metal surface, *J. Phys. Chem. Lett.*, 2019, **10**(7), 1574–1580.

52 M. Debiossac, A. Zugarramurdi, Z. Mu, P. Lunca-Popa, A. J. Mayne and P. Roncin, Helium diffraction on SiC grown graphene: Qualitative and quantitative descriptions with the hard-corrugated-wall model, *Phys. Rev. B*, 2016, **94**, 205403.

53 G. Vidali and C. Hutchings, Measurement of the Debye-Waller factor for He-LiF, *Phys. Rev. B: Condens. Matter Mater. Phys.*, 1988, **37**, 10374–10377.

54 K. H. Rieder and N. Garcia, Energy dependence and softness of the potential for He scattering from Ni(110), *Phys. Rev. Lett.*, 1982, **49**, 43–46.

55 Y. Ekinci and J. P. Toennies, Thermal expansion of the LiF(001) surface, *Surf. Sci.*, 2004, **563**(1), 127–134.

56 D. Farías, R. Miranda and K. H. Rieder, Energy dependence of diffractive and rotationally inelastic scattering of D_2 from NiAl(110), *J. Chem. Phys.*, 2002, **117**(5), 2255–2263.

57 D. M. Danailov, R. Pfandzelter, T. Igel, H. Winter and K. Gärtner, Test of the interatomic potential in the ev-region by glancing-angle scattering of He-atoms from Fe(001), *Appl. Surf. Sci.*, 2001, **171**(1), 113–119.

58 P. Kraus, A. Tamtögl, M. Mayrhofer-Reinhartshuber, F. Apolloner, Ch Gösweiner, S. Miret-Artés and W. E. Ernst, Surface structure of Bi(111) from helium atom scattering measurements. inelastic close-coupling formalism, *J. Phys. Chem. C*, 2015, **119**(30), 17235.

59 M. C. Schram and E. J. Heller, Approach to coherent interference fringes in helium-surface scattering, *Phys. Rev. A*, 2018, **98**, 022137.

12328 | *Phys. Chem. Chem. Phys.*, 2022, **24**, 12319–12328

This journal is © the Owner Societies 2022